CHEMISTRY OF MATERIALS

Open Access

pubs.acs.org/cm

Article

Discovery of Dual Ion-Electron Conductivity of Metal–Organic Frameworks via Machine Learning-Guided Experimentation

Robabeh Bashiri, Preston S. Lawson, Stewart He, Sadisha Nanayakkara, Kwangnam Kim, Nicholas S. Barnett, Vitalie Stavila, Farid El Gabaly, Jaydie Lee, Eric Ayars, and Monica C. So*

Cite This: *Chem. Mater.* 2025, 37, 1143–1153

Read Online

ACCESS | Metrics & More | Article Recommendations | Supporting Information

ABSTRACT: Identifying conductive metal–organic frameworks (MOFs) with a coupled ion-electron behavior from a vast array of existing MOFs offers a cost-effective strategy to tap into their potential in energy storage applications. This study employs classification and regression machine learning (ML) to rapidly screen the CoREMOF database and experimental methodologies to validate ML predictions. This process revealed the structure–property relationships contributing to MOFs' bulk ion-electron conductivity. Among the 60 conductive compounds predicted, only two p-type conductive MOFs, $[Cu_3(\mu_3\text{-}OH)(\mu_3\text{-}C_4H_2N_2O_2)_3(H_3O)]\cdot 2C_2H_5OH\cdot 4H_2O$ (**1**) and $NH_4[Cu_3(\mu_3\text{-}OH)\text{-}(\mu_3\text{-}C_4H_2N_2O_2)_3]\cdot 8H_2O$ or (**2**) ($C_4H_2N_2O$ = 1H-pyrazole-4-carboxylic acid), were validated for their coupled electron-ion behavior. MOFs utilize earth-abundant copper and pyrazoles as ligands, demonstrating significant potential following thorough electrochemical characterization. Further analysis confirmed the critical role of strong σ-donating, π-accepting, and redox-active ligands in promoting electron mobility. In-depth structural investigations revealed that the presence of the O–Cu–N chain significantly influences conductivity, outperforming MOFs with only Cu–N or Cu–O bonds. Additionally, this study highlights how higher ionic conductivity is correlated with the ion mobility through linkers in **1** or the presence of ammonium ions in **2**. These structure–property relationships offer valuable insights for future research in using ML coupled with experimentation to design MOFs containing earth-abundant reagents for ion-electron conductivity without employing a host–guest MOF strategy.

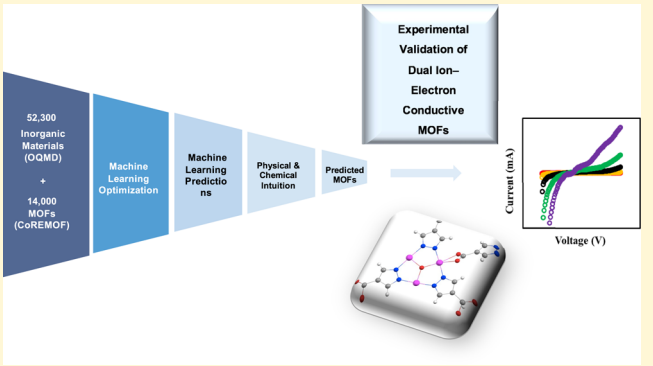

1. INTRODUCTION

As highly porous crystalline materials that consist of metal ions coordinated to organic donor linkers, metal–organic frameworks (MOFs) have extraordinary synthetic and chemical tunability. This modularity enables researchers to unlock their potential for electronic and optoelectronic devices[1−3] chemical sensors,[4] and energy conversion devices.[5] Electrical conductivity in MOFs is achieved through π-d orbital overlap between metal nodes and linkers, enabling electron delocalization.[6] Conversely, ionic conductivity is facilitated by functional groups like − OH, − NH_2, and − COOH, or molecular coordination at metal nodes, which enhance pore hydrophilicity and promote a hydrogen bonding network for effective proton migration.[7] However, given the limited orbital delocalization between metals and ligands in MOFs, this suppresses charge transfer.[8−10] To overcome the generally poor electrical conductivities (ca. 10^{-10} S·cm^{-1}) of a majority of MOFs,[11−13] researchers have designed intrinsically conductive MOFs with conjugated organic ligands and softer metal cations.[8,14−17] To promote ionic conductivity in MOFs, some have attempted to reduce void space and facilitate proton diffusion.[18−20] Recently, researchers reported that coupling ion and electron conductivities in MOFs facilitates rapid transport of both ions and electrons to the surface, enabling the entire surface area to act as active sites when used as cathode materials in fuel cells.[21] This dual functionality compares favorably to materials that exhibit only single ion or electrical conductivity, and can be considered a stepping stone for materials for energy storage applications, as they may in both excellent mass and charge transport, rendering the entire pore volume of materials accessible for charge storage at high rates. Few studies have reported on MOFs exhibiting coupled ion and electronic transport. Su et al.[22] demonstrated that redox-active ligands are a prerequisite in accessing dual ion-electron conductivity in the same MOF. Furthermore, Choi et al.[23]

Received: October 29, 2024
Revised: January 9, 2025
Accepted: January 10, 2025
Published: January 21, 2025

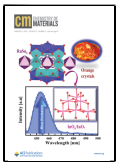

reported a zinc-based, dual-conductive MOF, designated as Zn-HHTP-H_2O, simultaneously conducting both electrons and protons. However, designing MOFs with coupled ion-electron conductivity in a predictable manner remains highly challenging due to a limited number of design principles guiding the development of these MOFs. To properly harness design principles, in-depth systematic studies of structure−property relationships in coupled ion-electron conductive MOFs are required. However, searching for conductive MOFs from the large numbers of MOF structures in databases is prohibitively time-and resource-intensive.

Therefore, a high-throughput computational screening approach using machine learning (ML) was chosen to search for MOFs with specific characteristics.[24] A literature survey has confirmed that there are some reports by He[25] and Rosen,[26] leveraging ML models to recommend promising MOF candidates with targeted electrical conductivity properties. Thus, these studies move toward employing ML to identify possible structural motifs for coupled ion-electron conductive MOFs with improved performance for practical applications, which have been neglected by researchers until now.

To elucidate the complex structure−property relationships that govern bulk ion-electron conductivity in MOFs, we have integrated machine learning (ML) with experimental analysis. This integrated approach is designed to tackle fundamental questions central to advancing the field: Which organic linkers and metal ions are common for coupled ion-electron transfer? What roles do charge-balancing counterions play in ionic and electrical conductivity? How do electrical properties predicted by ML compare with those validated experimentally, such as band gaps? What are the primary mechanisms of charge transport influencing MOF conductivity? This comprehensive analysis aims to shed light on the critical influences of linkers, metal ions, and counterions on the coupled ion-electron conductivity in MOFs, thereby offering insights that could redefine material design strategies in this promising area.

We rigorously trained four ML classification and regression models using ∼52,300 inorganic compounds in Open Quantum Materials Database (OQMD)[27] and screened 14,000 MOFs structures from the Computation Ready, Experimental Metal−Organic Framework (CoREMOF) database[28] using an ensemble voting method. Since the CoREMOF database lacks band gap properties, we adopted a regression analysis approach to predict the band gaps of the MOFs. Through ML analysis of the CoREMOF database, we identified 60 conductive MOFs. Out of these, 16 MOFs were chosen for experimental validation based on specific criteria, including a band gap energy (E_g) ranging between 0 and 2 eV, which optimizes potential electrical conductivity. Other factors considered were the availability of crystallographic information files (CIFs) and Digital Object Identifiers (DOIs) for each MOF, which are necessary to reproduce synthesis procedures and create accurate powder X-ray diffraction (PXRD) patterns. Additionally, we assessed the availability of starting materials for each selected MOF, as some are discontinued. The choice of copper as the metal source was further supported by a high percentage of predictions favoring copper-based MOFs, highlighting the common use of copper in MOF reactions and its role in influencing conductivity.

Consequently, experimentally validated data confirmed that only two MOFs ($[Cu_3(\mu_3{-}OH)\ (\mu_3{-}C_4H_2N_2O_2)_3(H_3O)]\cdot 2C_2H_5OH\cdot 4H_2O$ or **1** and $NH_4[Cu_3(\mu_3{-}OH)(\mu_3{-}C_4H_2N_2O_2)_3]\cdot 8H_2O$ or **2**, ($C_4H_2N_2O$ = 1H-pyrazole-4-carboxylic acid) are both ionically and electrically conductive. It is noteworthy to highlight that they were easily synthesized from earth abundant copper and pyrazole ligands. These two MOFs were previously evaluated solely for their roles in CO oxidation[29] and selective gas separation[30] which may have significant implications for cost-effective energy storage applications.

In this work, we build upon their seminal contributions by revealing previously overlooked but important structure−property relationships derived from ML and mechanisms derived from electrochemical measurements that are important for coupled ion-electron transfer. Our investigation further highlights how regression analysis can be useful for ranking the priority of ML-predicted MOFs to experimentally validate to save time and resources in the laboratory environment.

2. MODELING SECTION

2.1. Machine Learning. Our approach (Figure 1) utilizes ML methods known as classifiers to determine which compounds in the CoREMOF database are conductive. These models were implemented using the scikit-learn module[31] and trained using ∼52,300 inorganic compounds from OQMD. Once models were optimized, we screened over 14,000 MOF structures from the CoREMOFs database. Before screening CoREMOF, we removed any compounds with the following elements because of practical limitations in obtaining them: Fr, Ra, Ac, Th, Pa, U, Np, Pu, Am, *Cm*, Bk, Cf, Es, Fm, Md, No, Lr, Rf, Db, Sg, Bh, Hs, Mt, Ds, Rg, Cn, Nh, Fl, Mc, Lv, Ts, Og, Ce, Pr, Nd, *Pm*, Sm, Eu, Gd, Tb, Dy, Ho, Er, Tm, Yb, and Lu. Figure 1 represents our full screening pipeline.

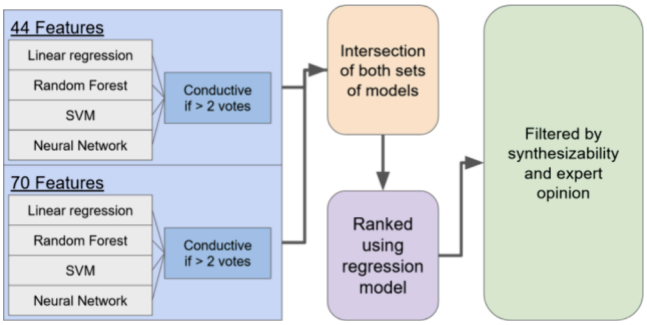

Figure 1. Overview of the ML process used to train and screen for electrically conductive compounds in OQMD. A voting-based ensemble method was used to combine the predictions made by four individual models. If two or more models voted "conductive", the compound was marked as conductive. We repeated this using both 44 and 70 feature models and took the intersection as our final result.

The training data was extracted from the compounds present in the OQMD that resembled MOFs. We only selected compounds from the OQMD database that contained over ten atoms in their chemical formula and at least one metal atom. These parameters for the selected training data were chosen to align the training data more closely with the MOF data we screened.[28] To build a ML model, we need to first build a training data set by labeling compounds as electrically conductive or nonconductive. To identify semiconductive compounds, we labeled compounds with E_g falling within the range of $0 < E_g \leq 1.5$ eV as positive, and all else were considered negative, creating a binary classification problem.

https://doi.org/10.1021/acs.chemmater.4c02974
Chem. Mater. 2025, 37, 1143−1153

The classification model will output a prediction, conductive or nonconductive, for each compound.

It is difficult to know how well a model trained on OQMD data will behave when making predictions on CoREMOF. There are no band gap values for compounds in CoREMOF, so there is no way to tell how well a model does on those compounds. Instead, we try to represent OQMD compounds in such a way that they resemble CoREMOF compounds, discussed in Section 2.2.1. We also divide OQMD into a training and test set such that the test set is like compounds in CoREMOF, creating a similarity split. We used a Ball Tree method to find compounds in OQMD that closely (measured using Euclidean distance) resembled CoREMOF compounds. We also created a random split with a 70/30 training to test ratio. We used 4-fold cross validation during training. Random and similarity split results are in Table S5. Figure 2 visualizes

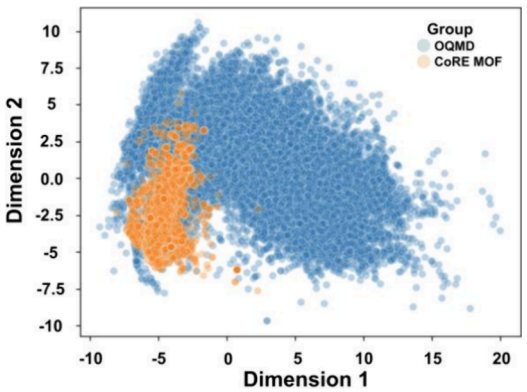

Figure 2. OQMD and CoREMOF samples are represented using 70 features and projected down to 2D space using PCA.

the distribution of the training set from OQMD, the testing set from OQMD, and the screening set from CoREMOF. The test set from OQMD overlaps with the screening set from CoREMOF, suggesting that compounds represented using 70 features resemble each other. We optimized several ML modeling methods, trained production models using all available OQMD data, and combined them into an ensemble using popular voting. The ensemble was then used to screen the CoREMOF database. Upon predicting electrically conductive MOFs, the important next step was to determine whether physical samples of those MOFs were, in fact, electrically conductive.[32]

2.2. Training Data. *2.2.1. Features.* Following the work done by He et al.,[25] we chose 14 elemental properties (i.e., atomic number, group number, period number, Pauling electronegativity, electron affinity, melting point, boiling point, density, ionization energy, Mullikan electronegativity, polarizability, thermal conductivity, electrical conductivity, and electrical resistivity) from RDKit.[33,34] The addition of electrical conductivity and resistivity is unintuitive, as they are the inverse of each other. However, adding both features showed more improvement over adding each individually. Mean decrease in impurity using the random forest model showed that electrical conductivity was more valuable than electrical resistivity and should be used if only one property were selected. Afterward, 5 statistical features, including maximum value, minimum value, standard deviation, mean, and geometric mean, were evaluated from the physical properties of each compound.

The properties and statistical features composed the input data used to build the ML model. This meant 70 total features for each compound for the training of all models. We experimented with removing low variance features, which reduced the number of features to 44. Overall model performance was not affected much (Table S5). Thus, only results from using 70 features are reported in Figure 2. To evaluate how similar OQMD and CoREMOF data sets were, principal component analysis (PCA) was used to find the top two eigenvectors and then project them down onto scatter plots (Figures S14−S16). In Figure 2, the PCA plot shows the spatial distribution of features exhibits some overlap, suggesting the potential for the band gap model to exhibit some predictive power for MOFs in some regions of feature space. The proximity of CoREMOF and OQMD samples in Figure 2 suggests that each CoREMOF sample has a similar neighbor in the OQMD data set. To get a quantifiable comparison, we calculated the silhouette scores which compares a sample's intracluster distance to the mean nearest-cluster distance. While the highest score is 1, in which samples are very close to the assigned cluster, a random clustering results in a score closer to 0. However, a silhouette score of 0.1463 was obtained in our case, suggesting that the models trained on OQMD may generalize to the CoREMOF model.

2.2.2. Classifiers. We used four types of classifiers: neural network (NN), random forest (RF), logistic regression (LR), and support vector machine (SVM). The LR model predicts probabilities directly through the logit transform and works best as a binary classifier. RF is an ensemble method that combines a series of decision trees. SVM finds a maximally separating N-1-dimensional manifold in N dimensional space. NNs use an iterative method to optimize a very high dimensional, nonlinear function given a loss function. Here, we defined a threshold of $0 < E_g \leq 1.5$ eV, where any material with E_g between 0 and 1.5 eV was labeled as conductive, while those with an energy gap above 1.5 eV were labeled as nonconductive. Since band gaps are only related to electrical conductivity, we used that information to build band gap models and predict electrically conductive MOFs. Unfortunately, there is no currently existing data in CoREMOF or OQMD databases to evaluate ionic conductivity.

2.2.3. Ensemble Voting Analysis. We used a voting-based ensemble method to combine the predictions made by individual models. Random forest, neural network, linear regression, and SVM models each placed a vote, then if two or more models voted "conductive", the compound was marked as conductive.[25,28] We repeated this using both 44 and 70 feature models and took the intersection as our final result. We trained a production model using the best set of hyperparameters from a random split and all available data. The production models were used to perform screening.

2.2.4. Regression Analysis. Ensemble voting resulted in more compounds than we could reasonably validate. Thus, to rank the MOFs classified as electrically conductive, we built a regression model to predict band gaps. We removed metals in the OQMD data set when training regression models. There are no metals in the CoREMOF data set and the band gap of any metal is cutoff at 0 in OQMD. After removing metals from OQMD, there remained 4923 test compounds and 11587 training compounds. We used the same features described in Section 2.2.1 and a five layer, fully connected neural network with a mean squared error loss. The regression model

https://doi.org/10.1021/acs.chemmater.4c02974
Chem. Mater. 2025, 37, 1143−1153

produced a predicted band gap for each CoREMOF compound between the values of 0 and 8. Since the regression models and classification models are completely independent of each other, they sometimes disagree; the regression model would predict E_g values outside of what we considered semiconductive. Regression is inherently harder since regression needs to predict a specific value, while classification only needs to be able to identify different classes. We trust in the ranking of each MOF's predicted band gap rather than the absolute value, so we only used it for ranking. We performed ranking with a model using 44 features since they outperformed models using 70 features. We then filtered the MOFs that were classified as electrically conductive and kept ones with a lower predicted band gap.

3. EXPERIMENTAL DATA VALIDATION SECTION

3.1. Synthesis of MOFs. A comprehensive list of 60 predicted electrically conductive CoREMOFs, complete with details such as organic ligands and metal ions, is available in Table S1 to S3. Out of the 60, we successfully synthesized and characterized 16 MOFs, but of the 60, only 2 MOFs demonstrated both ionic and electrical conductivity. Thus, we only outlined the synthesis and characterization procedures for the two MOFs, $[Cu_3(\mu_3{-}OH)(\mu_3{-}C_4H_2N_2O_2)_3]{\cdot}2C_2H_5OH{\cdot}4H_2O$[29] or **1**, and $NH_4[Cu_3(\mu_3{-}OH)(\mu_3{-}C_4H_2N_2O_2)_3]{\cdot}8H_2O$[30] or **2**. All utilized chemicals were procured from Fisher Scientific and Sigma-Aldrich, and they were used without additional purification.

3.1.1. Synthesis of ***1****.* 1H-pyrazole-4-carboxylic acid (H_2L) (0.2016 g, 1.8 mmol) and $Cu(NO_3)_2{\cdot}3H_2O$ (0.2898 g, 1.2 mmol) were dissolved in a mixed solvent of 12.0 mL DMF, 9.0 mL deionized water (DI), and 12.0 mL ethanol. The resulting reaction mixture was then transferred to a 50 mL Teflon-lined pressure vessel and heated to 80 °C for 72 h under autogenous pressure. After cooling to room temperature, the formation of dark blue crystals was observed, which were subsequently washed with DI water and filtered under vacuum.

3.1.2. Synthesis of ***2****.* H_2L (0.456 g, 4 mmol) and Cu $(NO_3)_2{\cdot}3H_2O$ (0.976 g, 4 mmol) were dissolved in a 60 mL solution of 15:1 aqueous ammonia. The reaction mixture was left at room temperature for 3 days, and then the resulting crystals were rinsed with DI water and filtered under vacuum to separate them from the remaining liquid.

3.2. Material Characterization. Powder X-ray diffraction (PXRD) analyses were performed to identify the crystalline structure of the material. These analyses were conducted using a Rigaku Geigerflex X-ray diffractometer, employing Cu Kα radiation. The diffraction data were collected over a range of 5° to 50° (2θ), with a step size of 0.02°.

To probe the molecular vibrational modes and identify various functional groups, Fourier-transform infrared spectroscopy (FTIR) was executed using a ThermoFisher Nicolet spectrometer with the spectral domain ranging from 4000 to 400 cm^{-1}. To investigate the oxidation states of the metals present, X-ray photoelectron spectroscopy (XPS) measurements were taken using an Omicron Model DAR400 instrument equipped with an Al Kα source, which emits photons at an energy of 1486.6 keV. The resultant photoelectrons were detected using a Physical Electronics Model 10−360 analyzer. For accuracy in our analysis, binding energies were calibrated with the C 1s peak at 285.0 eV. The interpretation of the XPS spectra involved a Shirley background subtraction and a fitting of the data to mixed Gaussian−Lorentzian (70/30) line shapes, using CasaXPS software.

Additionally, the optical properties, absorption edge, and optical band gap energy were investigated through diffuse reflectance spectroscopy (DRS). Employing an ASD Quality Spec Pro UV−vis spectrometer, equipped with a fiber optic mug light attachment, we captured detailed spectra in the range of 350 to 2500 nm. The E_g was determined by extrapolating the Tauc plot, which is a plot of $(F(R){\cdot}h\nu)^2$ versus photon energy ($h\nu$). The photon energy was calculated using the Planck-Einstein equation ($E = hc/\lambda$), where, h is Planck's constant = 4.13×10^{-15} eV·s, c is the speed of light = 2.99×10^8 m·s^{-1} and λ (nm) is wavelength.

The TEM experiments were conducted using a ThemIS transmission electron microscope operating at 300 keV, equipped with a Bruker SuperX energy dispersive X-ray spectroscopy (EDS) detector for rapid chemical identification.

3.3. Conductivity Measurements. These measurements were performed on both as-synthesized and vacuum-dried samples for all 16 synthesized MOFs. All pellets were prepared by compressing 40 mg of each MOF using a hydraulic press at 2.50 kPa for 4 min, yielding pellets of 0.96 cm in diameter and 0.10−0.20 cm in thickness. The conductivity measurements, as illustrated in Figure S1, were conducted using a four-wire resistance technique with a Keithley digital multimeter. Conductivities were calculated utilizing the eq 1:

$$\sigma = L/RA \tag{1}$$

where the conductivity (σ) depends on L, the path length of the current, R the measured resistance, and A the circular cross-sectional area of the cylindrical pellet.[35] Current−voltage (I−V) data were collected using a custom-written Python script; further details are in SI.

To investigate the electrical properties, a subset of the synthesized samples underwent activation at 80 °C for 15 h. This step was carried out to ensure the removal of any residual moisture and to enhance the accuracy of the electrical characterization.

Temperature-dependent conductivity measurements were performed to confirm semiconductor behaviors MOFs by wrapping the sample holder with resistive heating tape linked to a Digi-Sense standard temperature controller, accompanied by a J-type thermocouple. Data collection involved a ramp and soak method, spanning from 297 to 353 K. The temperature dependence of conductivities was analyzed using the Arrhenius eq 2, where E_a corresponds to the charge transport activation energy, k_B denotes the Boltzmann constant, and A is the pre-exponential factor.

$$\ln(\sigma) = \ln A - E_a/k_B T \tag{2}$$

We were also curious about whether and how ion conductivity will change under different relative humidities, from 30% to 98% RH; Figure S2 illustrates the setup. Furthermore, we investigated temperature-dependent conductivity measurements at various temperatures ranging from 298 to 353 K, with a focus on the 98% RH condition.

3.4. Electrochemical Measurements. To investigate future electrochemical behavior, measurements were performed on **1** and **2** by employing a Gamry 1010E electrochemical workstation equipped with a Frequency Response Analyzer (FRA) module. Cyclic voltammetry (CV) measurements were conducted with a three-electrode configuration under alkaline conditions (0.1 M KOH). The CVs were obtained utilizing a glassy carbon working electrode, a platinum wire as the auxiliary electrode, and an Ag/AgCl reference electrode. Data acquisition was performed at a scan rate of 100 mV·s^{-1}, spanning a potential window from −0.8 to 0.8 V. Further information on the preparation of the working electrodes for H_2L, and **1** and **2**, is available in the SI.

Electrochemical impedance spectroscopy (EIS) is a highly effective technique for studying the interaction between the electrode and electrolyte. The measurements were conducted over a frequency range of 0.1 Hz to 100 kHz, employing a two-electrode configuration with a signal amplitude of 10 mV. Instrument operation and data acquisition were controlled and monitored using Z-Plot/Z-View software. The impedance data were fitted using the GAMRY analyst software with the simplex algorithm.

Mott−Schottky (M-S) analysis is commonly conducted to measure capacitance as the potential varies in the system under depletion conditions. Equation 3 is employed to estimate the capacitance of the space charge at the depleted semiconductor electrode in the photoelectrode/electrolyte interface. This equation utilizes the real impedance (Z″) obtained from the impedance analyzer at a frequency of 1 kHz in dark conditions. By plotting $1/C^2$ against the applied potential, the M-S plot allows for extrapolation on the X-axis to

https://doi.org/10.1021/acs.chemmater.4c02974
Chem. Mater. 2025, 37, 1143−1153

determine the flat band potential (V_{fb}). The V_{fb} is represented by the point where $1/C^2$ equals zero.

$$C = 1/\pi f Z'' \quad (3)$$

4. RESULTS AND DISCUSSION

4.1. ML Predictions. We evaluated the four classifiers using the ratio of true positives versus all positive predictions, also known as precision. To calculate precision, predictions from the four classifiers were compared against DFT derived band gap calculations from OQMD. Precision results, after the hyperparameter search, are summarized in Table 1. We prioritized precision in our evaluation because laboratory experimentation is costly, and it was crucial to ensure that positive classifications were accurate rather than identifying all conductive MOFs.

Table 1. Summary of Conducting and Nonconducting Precision Values Trained Using 70 Features and a Random Split, after Their Respective Hyperparameter Searches

classifier	conducting precision	nonconducting precision
RF	0.90	0.81
SVM	0.89	0.80
NN	0.91	0.77
LR	0.86	0.73

To evaluate the accuracy of the regression model based on 70 features in predicting band gaps, we calculated R^2 and Spearman correlations. These are two values which provide information about the strength and relationship between the trained model and the testing model. Our model yields a R^2 score of 0.65 (Figure 3) and a Spearman correlation of 0.78.

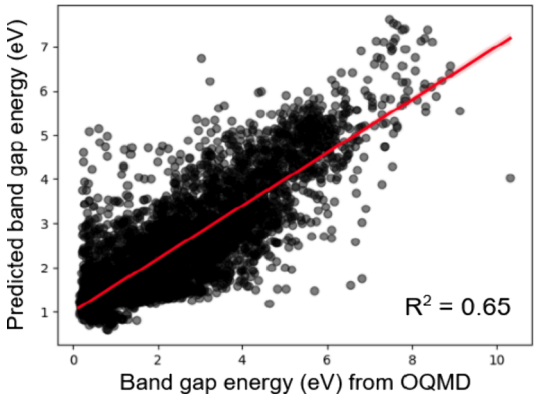

Figure 3. Summary of regression results for band gap from OQMD.

The R^2 score is consistent with model performance in fields like drug discovery,[36,37] and the Spearman correlation is sufficiently high. Despite the limited information in our features which were solely based on chemical formulas in OQMD and CoREMOF data sets, we were able to determine the priority of validation for electrical conductivity in our samples.

Table 2 summarizes the most common metal and organic ligand structural motifs of 60 MOFs predicted from four ML models. Interestingly, most of our predicted conductive MOFs exhibited copper metal ions. The frequent occurrence of copper in Table 2 is not only consistent with the conductive Cu−N coordinated MOFs,[38,39] but the conductive Cu−S coordinated MOFs with the reported electrical conductivity at 10.96 $S \cdot cm^{-1}$.[40,41] For the organic ligands, we prioritized ligands with strong σ-donating and π-accepting nature, such as pyrazoles. These characteristics promote higher electron mobility, which is a desirable and crucial aspect in conductive compounds. Though cyanides appeared most frequently in Table 1, they are weak π-acceptors, so we did not prioritize those MOFs. Further, since amines are only strong σ-donors and benzenes are only strong π donors, we ranked them lower in priority for experimental validation.

Table 2. Summary of Dominant Motifs Found in 60 Predicted Conductive MOFs

type of structure	structural motifs present[a]	% in predictions[b]
organic linker	azides	5.0
	pyrimidines	5.0
	pyridyls	5.0
	amines	8.3
	pyrazoles	8.3
	benzene	8.3
	cyanides	38
metal	Zn	3.0
	Co	5.0
	Cd	5.0
	W	7.0
	Re	8.3
	Mn	12
	Cu	70

[a]Percentages of ligands do not sum up to 100%, because some MOFs contain more than one ligand, and less frequently observed ligands have been excluded. [b]Percentages of metals do not add up to 100%, because some MOFs contain more than one metal, and less frequently observed metals have been excluded.

4.2. Experimental Data Validation Results. *4.2.1. Structural and Compositional Characterization.* Given the higher frequency of copper and pyrazole-containing MOFs, we prioritized MOFs with those structural motifs. However, we also considered the feasibility of their synthesis with commercially available reagents and literature methodologies, as well as whether the band gaps predicted by ML regression analysis fell below 2 eV in Table S1. This resulted in the prioritization of **1** and **2**.

Formation of structures of **1** and **2** are confirmed with PXRD patterns which match simulated patterns (Figure S4). As depicted in Figures 4a and 4b, both samples feature trinuclear planar structures, including $Cu_3(\mu_3{-}OH)$ cores. In these cores, each Cu (II) ion is coordinated by bridging nitrogen atoms from pyrazolyl groups and oxygen atoms from carboxyl groups of the ligands. The three Cu (II) ions are positioned at the vertices of the triangular units, with μ_3−OH ions from the solvents located nearly in the planes defined by the Cu(II) ions.[29] The space groups for **1** and **2** were $F\underline{4}3c$ and $Fd\underline{3}c$ space groups with Cu (II) coordination modes of four and five, respectively. This difference in space group and coordination is due to the presence of different solvents, different ratio of copper to H_2L, and reaction temperature and pressure during the preparation of MOFs.[30,42] Thus, compared to **1**, **2** has higher symmetry, characterized by tetrahedral cages with an inner diameter of approximately 12.5 Å. This larger size enables **2** to accommodate NH_4^+ and H_3O^+ ions more effectively.

https://doi.org/10.1021/acs.chemmater.4c02974
Chem. Mater. 2025, 37, 1143−1153

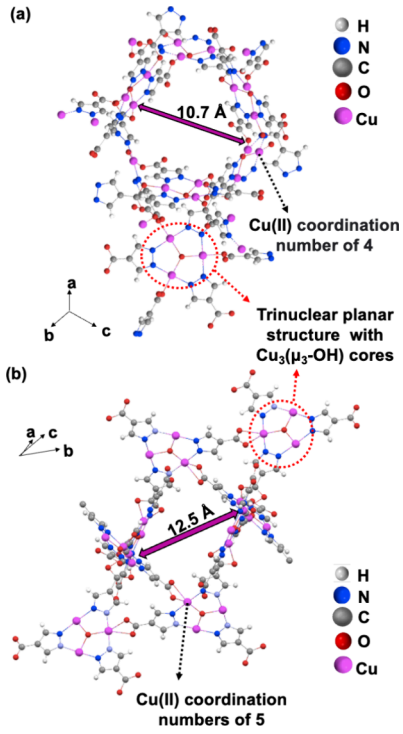

Figure 4. 2D view of crystal structures of (a) **1** and (b) **2**. The key molecular features are delineated by dotted lines, and the legend identifies atom types by color: hydrogen (H) in white, nitrogen (N) in blue, carbon (C) in black, oxygen (O) in red, and copper (Cu) in purple. The directional axes are also labeled, providing a reference for the molecular orientation in three-dimensional space.

When the MOFs form, the FTIR signals (Figure S6) corresponding to C = O (1680 cm^{-1}) and N−H (3270 cm^{-1}) vanish, while peaks associated with C−O and C−N aromatic stretching emerge at 1050 and 1280 cm^{-1}, respectively. These observations suggest the formation of Cu−N and Cu−O bonds with H_2L to form the expected MOFs.

XPS was employed to ascertain the oxidation states of copper within the samples. High-resolution XPS surveys (Figure S7) were conducted to analyze the spectral binding energies of copper, nitrogen, carbon, and oxygen orbitals for both **1** and **2**. The XPS spectra for Cu $2p_{3/2}$ (Figure S8) revealed a prominent peak at ∼935 eV, indicative of a + 2 oxidation state in $Cu(OH)_2$. The presence of characteristic shakeup satellite peaks in the range of 942 eV-945 eV confirms the existence of high-spin Cu(II) states.[43] The data suggest that both MOFs have undergone reduction, as evidenced by the XPS peaks at 932.88 and 932.70 eV (Figure S8) for **1** and **2**, respectively, corresponding to Cu(0) in the $2p_{3/2}$ orbital. The concentration of Cu (0) shows a stronger peak in **1** compared to **2**. This observation suggests hydrothermal reactions facilitated by H_2L or reactions with the solvent.[44−47] There are no signs of copper nanoparticles in either MOFs which may affect subsequent electrical characterization (Figure S13). Furthermore, this reduction aligns with the observed decrease in oxygen content in **1**, as indicated by the survey scan.

4.2.2. Optical and Electrical Properties. DRS data (Figure 5a) depict optical band gap energies of 1.4 and 1.38 eV for **1** and **2**, respectively, suggesting their semiconducting nature. The experimental E_g data align closely with the 1.33 eV predicted from regression analysis (Table S1).

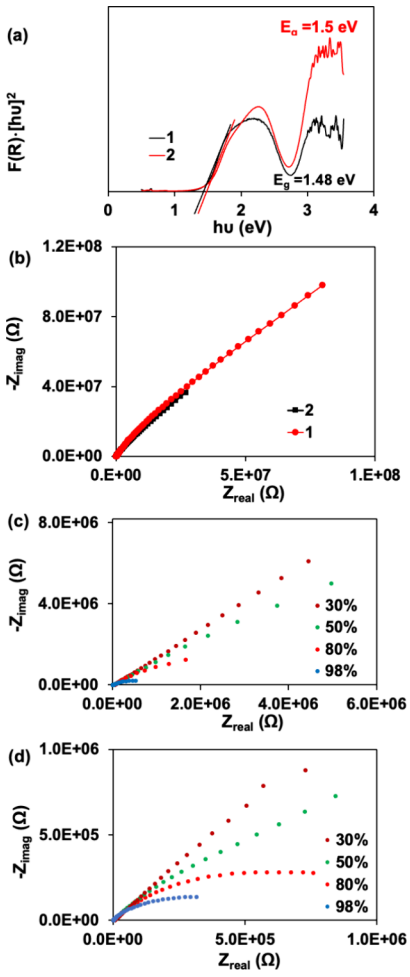

Figure 5. (a) Tauc plots and (b) Nyquist plots for **1** and **2** at room temperature. (c-d) Nyquist plots for **1** and **2** at 30%, 50%, 80%, and 98% humidity.

Further evaluating electrical properties, we measured the conductivity of these MOFs by employing eq 1. At room temperature (298 K), **1** and **2** exhibited conductivities of 7.26 × 10^{-9} S·cm^{-1} and 4.23 × 10^{-6} S·cm^{-1}, respectively. This conductivity is attributable to the π-d orbital overlap, facilitated by the H_2L linker's coordination with copper. The H_3O^+ and NH_4^+ ions play an important role in integration of multiple charge carrier species which are responsible for facile charge (ionic) transport. Significantly, **2** displayed higher conductivity than **1**, likely due to its anionic 3D porous framework that includes NH_4^+ cations and H_3O^+ crystallization molecules, as opposed to **1**, which only contains H_3O^+ cations.

To confirm their semiconducting properties, the temperature was increased from 298 to 353 K. We observed an increase in conductivity to 9.39 × 10^{-9} S·cm^{-1} and 5.97 × 10^{-6} S·cm^{-1}, for **1** and **2**, respectively.

The cyclic voltammogram of H_2L (Figure S9) in a 0.1 M KOH solution shows distinct redox processes: a reduction peak at −2.687 μA and 0.01 V, and an oxidation peak at 2.423 μA and 0.14 V vs Ag/AgCl reference electrode.[48] These peaks demonstrate the redox behavior of the H_2L linker, where the carboxylic group undergoes deprotonation in the alkaline environment to form a carboxylate anion ($-COO^-$), a stable redox species that engages in proton hopping.[49] This reversible redox action is key to the charge transport mechanism in the

https://doi.org/10.1021/acs.chemmater.4c02974
Chem. Mater. 2025, 37, 1143−1153

MOFs. To obtain a more detailed understanding of the charge transport dynamics in these MOFs, we employed EIS techniques. The Nyquist plots for **1** and **2** from EIS technique are depicted in Figure 5b. **2** exhibits a smaller semicircular arc compared to **1**, suggesting a reduced charge transfer resistance at its surface.[49,50] The experimental data fitted with the $[R_s(R_1Q)\ (R_2Q)\ ([R_3W]CR_4)]$ equivalent circuit (Figure S11) have been tabulated in Table S4.

Noticing that there are ammonium and hydronium cations in the structures of **1** and **2**, we wondered about the ionic conductivity of these MOFs. Thus, further investigation on the ionic conductivity was carried out by systematically varying the humidity from 30% to 98% for **1** and **2**. Nyquist plots (Figure 5c and 5d) indeed reveal that the diameter of the semicircles, indicative of resistance, reduces with increasing humidity. This suggests enhanced proton conductivity at high humidity levels. **1** shows a significant reduction in the diameters of the semicircles at different humidity levels, indicating that its proton conductivity is highly dependent on humidity. On the other hand, our findings for **2** reveal a more moderate reaction, with less noticeable changes in diameter by increasing concentrations of H_3O^+. This data confirms that the simultaneous presence of NH_4^+ and H_3O^+ results in reduced ion mobility on the surface of **2** compared to the presence of H_3O^+ alone in the sample **1**. This results from the elevated ion concentration and saturation with positive charges, leading to increased resistance to charge transfer. To gain insight into the proton conduction behavior, proton conductivities were measured by increasing temperature up to 353 K while maintaining a relative humidity of 98%. The highest proton conductivities for **1** and **2** were recorded 6.39×10^{-7} S·cm^{-1} and 5.3×10^{-7} S·cm^{-1} respectively at 353 K. The activation energy for **1** and **2** are found 0.91 and 0.95 meV, respectively, as presented in Figure 6a. The alignment in activation energies for both compounds are consistent with the Grötthuss mechanism typically associated with $E_a < 0.4$ eV.[22] The proton hopping likely occurs within the MOFs' pore channels in the presence of H_3O^+ in **1** and both H_3O^+ and NH_4^+ in **2**.

The electrical conductivities of **1** and **2** were measured for activated samples. Upon measurement at a temperature of 353 K, we observed conductivities of 1.55×10^{-8} S·cm^{-1} and 1.35×10^{-7} S·cm^{-1} for **1** and **2**, respectively. These results highlight a significant shift toward lower conductivity in the activated samples, marking a deviation from the predominantly ion conductivity patterns exhibited in humid environments. Furthermore, the I−V characteristics (Figures 6b and 6c) show that activated **1** and **2** exhibit increased current with the application of voltage across a range of temperatures, confirming their intrinsic electrical conductivity.[51] These plots also show that the activated samples generated less current at higher temperatures and potentials compared to the as-synthesized ones, confirming that proton transport is not the main mechanism of conductivity. On the other hand, the differences in conductivity between activated and as-synthesized samples can stem from partial pore collapse (Figure S5), which leads to structural distortions and disrupts conduction pathways.

Further analysis, leveraging XPS and CV, provided deeper insights into the changes in electrical conductivity mechanisms. The CV data (Figure S10) for **1** and **2**, particularly, revealed distinct cathodic peaks at −0.31 V and −0.24 V for 1 and 2, respectively. These peaks are indicative of the reduction process from Cu (II) to Cu(I), suggesting an active charge

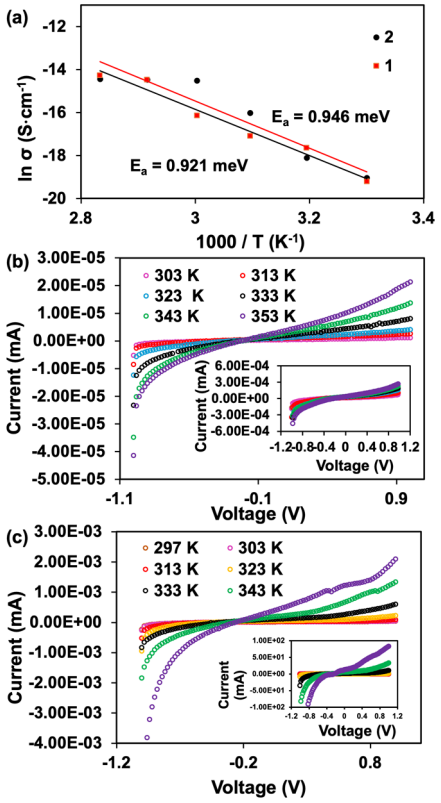

Figure 6. (a) Arrhenius plots for **1** and **2** at 98% RH as a function of temperature in the range of 297 K to 353 K of **1** and **2**. (b) and (c) current−voltage show characteristics of activated MOFs and as-synthesized (inset).

transfer process within the samples. The presence of mixed valence states of copper, specifically Cu (0), Cu(I), and Cu (II), as supported by the XPS data, plays a critical role in this phenomenon. The coordination of unsaturated Cu^{2+} sites within the structure exhibits significant charge transfer capabilities, contributing to the overall electrical conductivity. The mixed valence Cu (II)/Cu(I) enhances the charge density within the material and promotes charge delocalization. The delocalized charge moves through bond charge transport between the $Cu_3(\mu_3-OH)$ cores.[52,53] This alteration in the electronic structure after activation is a critical factor that dictates the electrical conductivity of the samples, marking a stark contrast to their behavior in proton conductivity under humid conditions. These findings not only shed light on the intrinsic properties of the materials but also underscore the importance of environmental factors in determining their conductive behavior.

The Mott−Schottky (M-S) analysis further explains the electrical properties of **1** and **2**, extending the I−V characteristics previously discussed. The M-S plots (Figure 7a and 7b) depict p-type behavior with a negative slope and a flat band potential (V_{fb}) of 0.61 V for **1** and 0.9 V for **2**.[54,55] The p-type conductivity identified by the M-S analysis aligns with the enhanced electrical conductivity evident in the I−V characteristics, which showed a consistent increase in current with applied voltage across various temperatures, indicative of hole conduction as the dominant mechanism after activation. The lower slopes present in **2** suggest a higher donor density and a reduced recombination rate, which is in harmony with the higher conductivities observed in the I−V tests and

https://doi.org/10.1021/acs.chemmater.4c02974
Chem. Mater. 2025, 37, 1143−1153

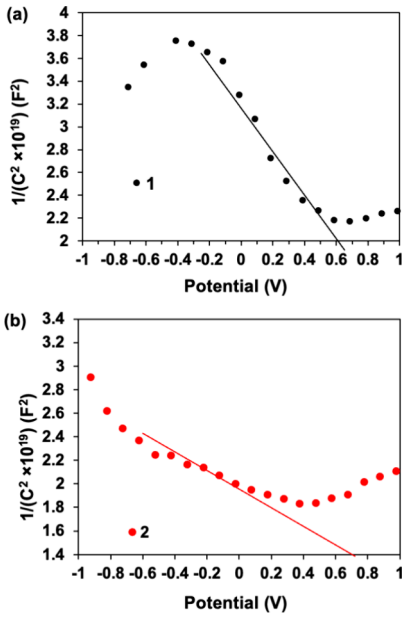

Figure 7. M-S plots for activated (a) **1** and (b) **2**.

substantiated by EIS findings.[56] These p-type semiconductors can enable the creation of hole-transporting layers with high stability.[57]

A comparison with other copper-based MOFs (Table 3) reveals that **1** and **2** exhibit 5−6 orders of magnitude higher electrical conductivities compared to single copper−oxygen or copper−nitrogen coordinated MOFs without requiring dopants[12,58] or undergoing redox reactions[59] due to the stronger π-d orbital interaction between Cu(II) and H_2L in **1** and **2**. The improved conductivities observed in these MOFs can be rationalized through the presence of a N−Cu−O heterostructure bonding configuration within the trinuclear planar framework, constituting a distinctive structural motif. The heightened electrophilicity of the oxygen atom within the N−Cu−O heterostructure, characterized by reduced Cu 3d electron density, fosters enhanced through-bond charge transfer along the trinuclear core (Figure S11).[60] This phenomenon results in improved conductivity when compared with conventional Cu−O and Cu−N bonding configurations.[61,62]

Table 3. Comparison of Conductivity Values of Selected MOFs Containing Copper−Oxygen and Copper−Nitrogen Coordination Bonds[a]

MOFs	σ (S·cm^{-1}) at RT	E_a (eV)	E_g (eV)	ref
1-activated	2.97× 10^{-8}	1.78 × 10^{-4}	1.4	this work
2-activated	5.91 × 10^{-9}	1.3 × 10^{-4}	1.5	this work
$Cu(TZ)_2$-activated	3.2 × 10^{-14}	0.59	2.3[14]	14
$Cu_2(DOBD)_2$	1.4 × 10^{-14}	0.69	2.2	14
$Cu_3(HHB)_2$	7.3× 10^{-8}	0.46	N/A	59
Cu-TATAB	9.75 × 10^{-12}			63

[a]H_2L: 1H-pyrazole-4-carboxylic acid, DOBDC: 2,5-dioxidobenzene-1,4-dicarboxylate, TZ: 1,2,3-triazolate, HHB: hexahydroxybenzene, H_3TATAB: 4,4′,4″-((1,3,5-Triazine-2,4,6-triyl)tris(azanediyl)) tribenzoic acid.

5. CONCLUSIONS AND OUTLOOK

In summary, we began by evaluating 14,000 MOFs using four ML models, leading to the identification of 60 conductive MOFs. Out of these, 16 MOFs were selected for experimental validation, based on band gap range and the accessibility of starting materials and synthetic methodologies. Among these, only two MOFs, featuring copper and pyrazoles, exhibited dual ion-electron conductivities, highlighting the importance of strong σ-donating, π-accepting, and redox-active ligands in promoting electron delocalization and mobility. Further, the N−Cu−O heterostructure bonding configuration is important in enhancing electrical conductivity. Importantly, higher ionic conductivity through the Grötthuss mechanism is correlated with the capacity for the linkers to promote proton mobility through the ligands in **1** or presence of ions (like NH_4^+) in **2**. The ML models were instrumental in elucidating structure−property relationships in copper-based MOFs showing dual ion-electron behavior. This endeavor also showcased the preliminary use of regression analysis for prioritizing which MOFs to experimentally validate.

These two p-type MOFs further demonstrated electrical conductivity significantly higher than that of other copper−oxygen and copper−nitrogen-based MOFs. EIS data revealed lower charge transfer resistance and recombination rates, particularly for the MOF with higher positive charge carrier densities. Comprehensive electrochemical studies, including MS and EIS, offered insights into charge carriers and transfer resistance, areas previously underexplored in studies of intrinsically conductive MOFs.

Validating machine learning data through experimentation additionally revealed challenges hindering the synthesis of proposed compounds, including:

1. Limited literature data: Some compounds lack documented literature, complicating confirmation of existence and properties.
2. Synthetic challenges: Certain MOFs pose synthetic difficulties due to discontinued precursors or inadequate methodological details, impacting reproducibility.
3. Cost and time constraints: MOF synthesis proves expensive and time-consuming due to low yields, intricate ligand syntheses, toxic chemicals, and prolonged drying. These challenges could limit scalability.

This research marks a significant step toward designing conductive MOFs with enhanced electronic and ionic conductivity, facilitated by strong σ-donating, π-accepting, and redox-active pyrazole-based ligands, O−Cu−N coordination, and proton mobility through MOF ligands and ions. Our findings emphasize the importance of experimental validation of ML predictions, accelerating the discovery and characterization of conductive MOFs for potential battery applications.

■ ASSOCIATED CONTENT

Supporting Information

The Supporting Information is available free of charge at https://pubs.acs.org/doi/10.1021/acs.chemmater.4c02974.

CoREMOFs synthesized from predicted conductive MOFs, conductivity setup details, Python script, electronic band and projected density of state (PDOS), PXRD of 1 and 2, FTIR and XPS of 1 and 2, cyclic voltammetry, equivalent circuit fitting, N−Cu−O heterostructure, TEM of 1 and 2 and machine learning results (PDF)

https://doi.org/10.1021/acs.chemmater.4c02974
Chem. Mater. 2025, 37, 1143−1153

AUTHOR INFORMATION

Corresponding Author

Monica C. So − *Department of Chemistry and Biochemistry, California State University, Chico, California 95929-0210, United States;* orcid.org/0000-0002-9044-4806; Email: mso@csuchico.edu

Authors

Robabeh Bashiri − *Department of Chemistry and Biochemistry, California State University, Chico, California 95929-0210, United States*

Preston S. Lawson − *Department of Chemistry and Biochemistry, California State University, Chico, California 95929-0210, United States;* orcid.org/0009-0008-7224-8335

Stewart He − *Lawrence Livermore National Laboratory, Livermore, California 95064-9234, United States*

Sadisha Nanayakkara − *Department of Chemistry and Biochemistry, California State University, Chico, California 95929-0210, United States*

Kwangnam Kim − *Lawrence Livermore National Laboratory, Livermore, California 95064-9234, United States;* orcid.org/0000-0003-1149-1733

Nicholas S. Barnett − *Department of Physics, University of Illinois, Chicago, Illinois 60607, United States*

Vitalie Stavila − *Sandia National Laboratories, Livermore, California 94551, United States;* orcid.org/0000-0003-0981-0432

Farid El Gabaly − *Sandia National Laboratories, Livermore, California 94551, United States;* orcid.org/0000-0002-5822-9938

Jaydie Lee − *College of Natural Sciences, California State University, Chico, California 95929-0210, United States*

Eric Ayars − *Department of Physics, California State University, Chico, California 95929-0210, United States*

Complete contact information is available at: https://pubs.acs.org/10.1021/acs.chemmater.4c02974

Author Contributions

R.B. and P.S.L carried out the experiments, wrote, and revised the manuscript. S.H. developed the models for ML work and wrote the ML sections, and N.S.B. edited the sections. S.N. and K.K. performed DFT calculations. V.S. and F.E.G collected and interpreted XPS data and revised the manuscript. J.L. fabricated the conductivity measurement setups and assisted us in troubleshooting the equipment. E.A. wrote the Python script for I−V measurement characterization. M.C.S. conceived the original idea, supervised the project, wrote, and revised the manuscript.

Notes

The authors declare no competing financial interest.

ACKNOWLEDGMENTS

R.B., P.S.L., and M.C.S. acknowledge the National Science Foundation (DMR-2137915). N.S.B. thanks CSU Chico's Lantis University Foundation for financial support. M.C.S. acknowledges support from Camille and Henry Dreyfus Foundation (TH-23-035) and U.S. Department of Energy, Office of Science, Offices of Basic Energy Sciences and Electricity under contract DE-SC0024581. Work at the Molecular Foundry (MF) was supported by the Office of Science, Office of Basic Energy Sciences, of the U.S. Department of Energy under Contract No. DE-AC02-05CH11231. We thank Tracy Mattox for DRS assistance and Qi Zheng and Haimei Zheng for HRTEM assistance from MF. Funding for this project was also provided by the Sandia Laboratory Directed Research and Development (LDRD) Program. Sandia National Laboratories is a multimission laboratory managed and operated by the National Technology & Engineering Solutions of Sandia, LLC, a wholly owned subsidiary of Honeywell International Inc., for the U.S. Department of Energy's National Nuclear Security Administration under contract DE-NA0003525. The work of K.K. was performed under the auspices of the U.S. DOE by the Lawrence Livermore National Laboratory (Contract No. DE-AC52-07NA27344). A part of this research used resources of the Oak Ridge Leadership Computing Facility at the Oak Ridge National Laboratory via the SummitPlus program, which is supported by the Office of Science of the U.S. Department of Energy under Contract No. DE-AC05-00OR22725. We thank Liwen Wan in part for the computational resources used in this work.

REFERENCES

(1) Allendorf, M. D.; Schwartzberg, A.; Stavila, V.; Talin, A. A. A Roadmap to Implementing Metal-Organic Frameworks in Electronic Devices: Challenges and Critical Directions. *Chem. - Eur. J.* **2011**, *17* (41), 11372−11388.

(2) Stavila, V.; Talin, A. A.; Allendorf, M. D. MOF-Based Electronic and Opto-Electronic Devices. *Chem. Soc. Rev.* **2014**, *43* (16), 5994−6010.

(3) D'Alessandro, D. M.; Kanga, J. R. R.; Caddy, J. S. Towards Conducting Metal-Organic Frameworks. *Aust. J. Chem.* **2011**, *64* (6), 718.

(4) Kreno, L. E.; Leong, K.; Farha, O. K.; Allendorf, M.; Van Duyne, R. P.; Hupp, J. T. Metal−Organic Framework Materials as Chemical Sensors. *Chem. Rev.* **2012**, *112* (2), 1105−1125.

(5) Park, H. J.; So, M. C.; Gosztola, D. J.; Wiederrecht, G. P.; Emery, J.; Martinson, A. B. F.; Er, S.; Wilmer, C. E.; Vermeulen, N. E.; Aspuru-Guzik, A.; Stoddart, J. F.; Farha, O. K.; Hupp, J. T. Layer-by-Layer Assembled Films of Perylene Diimide- and Squaraine-Containing Metal-Organic Framework-like Materials: Solar Energy Capture and Directional Energy Transfer. *ACS Appl. Mater. Interfaces* **2016**, *8*, 24983.

(6) Calvo, J. J.; Angel, S. M.; So, M. C. Charge Transport in Metal-Organic Frameworks for Electronics Applications. *APL Mater.* **2020**, *8* (5), No. 050901.

(7) Sadakiyo, M.; Yamada, T.; Kitagawa, H. Rational Designs for Highly Proton-Conductive Metal−Organic Frameworks. *J. Am. Chem. Soc.* **2009**, *131* (29), 9906−9907.

(8) Takaishi, S.; Hosoda, M.; Kajiwara, T.; Miyasaka, H.; Yamashita, M.; Nakanishi, Y.; Kitagawa, Y.; Yamaguchi, K.; Kobayashi, A.; Kitagawa, H. Electroconductive Porous Coordination Polymer $Cu[Cu(Pdt)_2]$ Composed of Donor and Acceptor Building Units. *Inorg. Chem.* **2009**, *48* (19), 9048−9050.

(9) Liu, L.; Xu, Q.; Zhu, Q. Electrically Conductive Metal−Organic Frameworks for Electrocatalytic Applications. *Adv. Energy Sustain Res.* **2021**, *2* (11), 2100100.

(10) Leong, C. F.; Usov, P. M.; D'Alessandro, D. M. Intrinsically Conducting Metal−Organic Frameworks. *MRS Bull.* **2016**, *41* (11), 858−864.

(11) Khatun, A.; Yadav, A.; Zhang, S.; Saha, S. Transforming an Insulating Metal−Organic Framework into Electrically Conducting Metal−Organic Framework⊃conducting Polymer Composites. *Materials Today Chemistry* **2022**, *24*, No. 100981.

(12) Angel, S. M.; Barnett, N. S.; Talin, A. A.; Foster, M. E.; Stavila, V.; Allendorf, M. D.; So, M. C. From insulator to semiconductor: Effect of host-guest interactions on charge transport in M-MOF-74 metal-organic frameworks. *J. Mater. Chem. C* **2024**, *12*, 2699−2704.

(13) Yoon, S.; Talin, A. A.; Stavila, V.; Mroz, A. M.; Bennett, T. D.; He, Y.; Keen, D. A.; Hendon, C. H.; Allendorf, M. D.; So, M. C. From N- to p-Type Material: Effect of Metal Ion on Charge Transport in Metal−Organic Materials. *ACS Appl. Mater. Interfaces* **2021**, *13* (44), 52055−52062.
(14) Sun, L.; Hendon, C. H.; Park, S. S.; Tulchinsky, Y.; Wan, R.; Wang, F.; Walsh, A.; Dincă, M. Is Iron Unique in Promoting Electrical Conductivity in MOFs? *Chem. Sci.* **2017**, *8* (6), 4450−4457.
(15) Park, S. S.; Hontz, E. R.; Sun, L.; Hendon, C. H.; Walsh, A.; Van Voorhis, T.; Dincă, M. Cation-Dependent Intrinsic Electrical Conductivity in Isostructural Tetrathiafulvalene-Based Microporous Metal−Organic Frameworks. *J. Am. Chem. Soc.* **2015**, *137* (5), 1774−1777.
(16) Sun, L.; Hendon, C. H.; Minier, M. A.; Walsh, A.; Dincă, M. Million-Fold Electrical Conductivity Enhancement in Fe_2 (DEBDC) versus Mn_2 (DEBDC) (E = S, O). *J. Am. Chem. Soc.* **2015**, *137* (19), 6164−6167.
(17) Gándara, F.; Uribe-Romo, F. J.; Britt, D. K.; Furukawa, H.; Lei, L.; Cheng, R.; Duan, X.; O'Keeffe, M.; Yaghi, O. M. Porous, Conductive Metal-Triazolates and Their Structural Elucidation by the Charge-Flipping Method. *Chem. - Eur. J.* **2012**, *18* (34), 10595−10601.
(18) Zhang, G.; Jin, L.; Zhang, R.; Bai, Y.; Zhu, R.; Pang, H. Recent Advances in the Development of Electronically and Ionically Conductive Metal-Organic Frameworks. *Coord. Chem. Rev.* **2021**, *439*, No. 213915.
(19) Horike, S.; Umeyama, D.; Kitagawa, S. Ion Conductivity and Transport by Porous Coordination Polymers and Metal−Organic Frameworks. *Acc. Chem. Res.* **2013**, *46* (11), 2376−2384.
(20) Kharod, R. A.; Andrews, J. L.; Dincă, M. Teaching Metal-Organic Frameworks to Conduct: Ion and Electron Transport in Metal-Organic Frameworks. *Annu. Rev. Mater. Res.* **2022**, *52* (1), 103−128.
(21) Song, Y.; Chen, Y.; Wang, W.; Zhou, C.; Zhong, Y.; Yang, G.; Zhou, W.; Liu, M.; Shao, Z. Self-Assembled Triple-Conducting Nanocomposite as a Superior Protonic Ceramic Fuel Cell Cathode. *Joule* **2019**, *3* (11), 2842−2853.
(22) Su, J.; He, W.; Li, X.-M.; Sun, L.; Wang, H.-Y.; Lan, Y.-Q.; Ding, M.; Zuo, J.-L. High Electrical Conductivity in a 2D MOF with Intrinsic Superprotonic Conduction and Interfacial Pseudo-Capacitance. *Matter* **2020**, *2* (3), 711−722.
(23) Choi, J. Y.; Stodolka, M.; Kim, N.; Pham, H. T. B.; Check, B.; Park, J. 2D Conjugated Metal-Organic Framework as a Proton-Electron Dual Conductor. *Chem.* **2023**, *9* (1), 143−153.
(24) Liang, H.; Jiang, K.; Yan, T.-A.; Chen, G.-H. XGBoost: An Optimal Machine Learning Model with Just Structural Features to Discover MOF Adsorbents of Xe/Kr. *ACS omega* **2021**, *6* (13), 9066−9076.
(25) He, Y.; Cubuk, E. D.; Allendorf, M. D.; Reed, E. J. Metallic Metal−Organic Frameworks Predicted by the Combination of Machine Learning Methods and Ab Initio Calculations. *J. Phys. Chem. Lett.* **2018**, *9* (16), 4562−4569.
(26) Rosen, A. S.; Iyer, S. M.; Ray, D.; Yao, Z.; Aspuru-Guzik, A.; Gagliardi, L.; Notestein, J. M.; Snurr, R. Q. Machine Learning the Quantum-Chemical Properties of Metal−Organic Frameworks for Accelerated Materials Discovery. *Matter* **2021**, *4* (5), 1578−1597.
(27) Kirklin, S.; Saal, J. E.; Meredig, B.; Thompson, A.; Doak, J. W.; Aykol, M.; Rühl, S.; Wolverton, C. The Open Quantum Materials Database (OQMD): Assessing the Accuracy of DFT Formation Energies. *npj Comput. Mater.* **2015**, *1* (1), 15010.
(28) Chung, Y. G.; Haldoupis, E.; Bucior, B. J.; Haranczyk, M.; Lee, S.; Zhang, H.; Vogiatzis, K. D.; Milisavljevic, M.; Ling, S.; Camp, J. S.; Slater, B.; Siepmann, J. I.; Sholl, D. S.; Snurr, R. Q. Advances, Updates, and Analytics for the Computation-Ready, Experimental Metal−Organic Framework Database: CoRE MOF 2019. *J. Chem. Eng. Data* **2019**, *64* (12), 5985−5998.
(29) Su, S.; Zhang, Y.; Zhu, M.; Song, X.; Wang, S.; Zhao, S.; Song, S.; Yang, X.; Zhang, H. An Active-Site-Accessible Porous Metal−Organic Framework Composed of Triangular Building Units: Preparation, Catalytic Activity and Magnetic Property. *Chem. Commun.* **2012**, *48* (90), 11118.
(30) Quartapelle Procopio, E.; Linares, F.; Montoro, C.; Colombo, V.; Maspero, A.; Barea, E.; Navarro, J. A. R. Cation-Exchange Porosity Tuning in Anionic Metal-Organic Frameworks for the Selective Separation of Gases and Vapors and for Catalysis. *Angew. Chem., Int. Ed.* **2010**, *49* (40), 7308−7311.
(31) Pedregosa, F.; Varoquaux, G.; Gramfort, A.; Michel, V.; Thirion, B.; Grisel, O.; Blondel, M.; Prettenhofer, P.; Weiss, R.; Dubourg, V.; Vanderplas, J.; Passos, A.; Cournapeau, D.; Brucher, M.; Perrot, M.; Duchesnay, É. Scikit-Learn: Machine Learning in Python. *J. Mach. Learn. Res.* **2011**, *12* (85), 2825−2830.
(32) Sheberla, D.; Sun, L.; Blood-Forsythe, M. A.; Er, S.; Wade, C. R.; Brozek, C. K.; Aspuru-Guzik, A.; Dincă, M. High Electrical Conductivity in Ni_3 (2,3,6,7,10,11-Hexaiminotriphenylene) $_2$, a Semiconducting Metal−Organic Graphene Analogue. *J. Am. Chem. Soc.* **2014**, *136* (25), 8859−8862.
(33) Landrum, G. *Rdkit: Open-Source Cheminformatics Software*; 2016.
(34) Landrum, G.; Tosco, P.; Kelley, B.; Sriniker; Gedeck; NadineSchneider; Vianello, R.; Ric; Dalke, A.; Cole, B.; AlexanderSavelyev; Swain, M.; Turk, S.; N, D.; Vaucher, A.; Kawashima, E.; Wójcikowski, M.; Probst, D.; Godin, G.; Cosgrove, D.; Pahl, A.; JP; Berenger, F.; Strets123; JLVarjo; O'Boyle, N.; Fuller, P.; Jensen, J. H.; Sforna, G.; DoliathGavid *rdkit/rdkit: 2020_03_1 (Q1 2020) Release*; Zenodo: 2020. .
(35) Li, H.; Liu, Y.; Liu, S.; Li, P.; Zhang, H.; Zhang, C.; He, C. High-Performance Polyaniline-Coated Carbon Nanotube Yarns for Wearable Thermoelectric Generators. *ACS Appl. Mater. Interfaces* **2024**, *16* (14), 17598−17606.
(36) Minnich, A. J.; McLoughlin, K.; Tse, M.; Deng, J.; Weber, A.; Murad, N.; Madej, B. D.; Ramsundar, B.; Rush, T.; Calad-Thomson, S.; Brase, J.; Allen, J. E. AMPL: A Data-Driven Modeling Pipeline for Drug Discovery. *J. Chem. Inf. Model.* **2020**, *60* (4), 1955−1968.
(37) Stevenson, G. A.; Jones, D.; Kim, H.; Bennett, W. F. D.; Bennion, B. J.; Borucki, M.; Bourguet, F.; Epstein, A.; Franco, M.; Harmon, B.; He, S.; Katz, M. P.; Kirshner, D.; Lao, V.; Lau, E. Y.; Lo, J.; McLoughlin, K.; Mosesso, R.; Murugesh, D. K.; Negrete, O. A.; Saada, E. A.; Segelke, B.; Stefan, M.; Torres, M. W.; Weilhammer, D.; Wong, S.; Yang, Y.; Zemla, A.; Zhang, X.; Zhu, F.; Lightstone, F. C.; Allen, J. E. High-Throughput Virtual Screening of Small Molecule Inhibitors for SARS-CoV-2 Protein Targets with Deep Fusion Models. In *Proceedings of the International Conference for High Performance Computing, Networking, Storage and Analysis*; ACM: St. Louis Missouri, 2021; pp 1−13. .
(38) Chen, T.; Dou, J.-H.; Yang, L.; Sun, C.; Libretto, N. J.; Skorupskii, G.; Miller, J. T.; Dincă, M. Continuous Electrical Conductivity Variation in M_3 (Hexaiminotriphenylene) $_2$ (M = Co, Ni, Cu) MOF Alloys. *J. Am. Chem. Soc.* **2020**, *142* (28), 12367−12373.
(39) Chen, K.; Ray, D.; Ziebel, M. E.; Gaggioli, C. A.; Gagliardi, L.; Marinescu, S. C. Cu[Ni(2,3-Pyrazinedithiolate) $_2$] Metal−Organic Framework for Electrocatalytic Hydrogen Evolution. *ACS Appl. Mater. Interfaces* **2021**, *13* (29), 34419−34427.
(40) Pathak, A.; Shen, J.-W.; Usman, M.; Wei, L.-F.; Mendiratta, S.; Chang, Y.-S.; Sainbileg, B.; Ngue, C.-M.; Chen, R.-S.; Hayashi, M.; Luo, T.-T.; Chen, F.-R.; Chen, K.-H.; Tseng, T.-W.; Chen, L.-C.; Lu, K.-L. Integration of a (−Cu−S−)n Plane in a Metal−Organic Framework Affords High Electrical Conductivity. *Nat. Commun.* **2019**, *10* (1), 1721.
(41) Ramaswamy, P.; Wong, N. E.; Shimizu, G. K. H. MOFs as Proton Conductors − Challenges and Opportunities. *Chem. Soc. Rev.* **2014**, *43* (16), 5913−5932.
(42) Blatov, V. A.; O'Keeffe, M.; Proserpio, D. M. Vertex-, Face-, Point-, Schläfli-, and Delaney-Symbols in Nets, Polyhedra and Tilings: Recommended Terminology. *CrystEngComm* **2010**, *12* (1), 44−48.
(43) Jiang; Sun; Zhao; Huo; Cui. A Flexible Portable Glucose Sensor Based on Hierarchical Arrays of Au@Cu(OH)2 Nanograss. *Sensors* **2019**, *19* (22), 5055.

https://doi.org/10.1021/acs.chemmater.4c02974
Chem. Mater. 2025, 37, 1143−1153

(44) Fan, H. Y. Temperature Dependence of the Energy Gap in Semiconductors. *Phys. Rev.* **1951**, *82* (6), 900−905.
(45) Albaladejo-Fuentes, V.; López-Suárez, F. E.; Sánchez-Adsuar, M. S.; Illán-Gómez, M. J. BaTi1−xCuxO3 Perovskites: The Effect of Copper Content in the Properties and in the NOx Storage Capacity. *Applied Catalysis A: General* **2014**, *488*, 189−199.
(46) Tu, B.; Pang, Q.; Xu, H.; Li, X.; Wang, Y.; Ma, Z.; Weng, L.; Li, Q. Reversible Redox Activity in Multicomponent Metal−Organic Frameworks Constructed from Trinuclear Copper Pyrazolate Building Blocks. *J. Am. Chem. Soc.* **2017**, *139* (23), 7998−8007.
(47) Biela, M.; Kleinová, A.; Klein, E. Phenolic Acids and Their Carboxylate Anions: Thermodynamics of Primary Antioxidant Action. *Phytochemistry* **2022**, *200*, No. 113254.
(48) Collyer, S. D.; Davis, F.; Higson, S. P. J. Sonochemically Fabricated Microelectrode Arrays for Use as Sensing Platforms. *Sensors* **2010**, *10* (5), 5090−5132.
(49) O'Mahony, A. M.; Silvester, D. S.; Aldous, L.; Hardacre, C.; Compton, R. G. Effect of Water on the Electrochemical Window and Potential Limits of Room-Temperature Ionic Liquids. *J. Chem. Eng. Data* **2008**, *53* (12), 2884−2891.
(50) Zhao, Z.; Kong, Y.; Huang, G.; Liu, C.; You, C.; Xiao, Z.; Zhu, H.; Tan, J.; Xu, B.; Cui, J.; Liu, X.; Mei, Y. Area-Selective and Precise Assembly of Metal Organic Framework Particles by Atomic Layer Deposition Induction and Its Application for Ultra-Sensitive Dopamine Sensor. *Nano Today* **2022**, *42*, No. 101347.
(51) Yadav, A.; Panda, D. K.; Zhang, S.; Zhou, W.; Saha, S. Electrically Conductive 3D Metal−Organic Framework Featuring π-Acidic Hexaazatriphenylene Hexacarbonitrile Ligands with Anion−π Interaction and Efficient Charge-Transport Capabilities. *ACS Appl. Mater. Interfaces* **2020**, *12* (36), 40613−40619.
(52) Roach, B. D.; Forgan, R. S.; Kamenetzky, E.; Parsons, S.; Plieger, P. G.; White, F. J.; Woodhouse, S.; Tasker, P. A. From Gas Phase Observations to Solid State Reality: The Identification and Isolation of Trinuclear Salicylaldoximato Copper Complexes. *Molecules* **2022**, *27* (19), 6421.
(53) Okubo, T.; Anma, H.; Tanaka, N.; Himoto, K.; Seki, S.; Saeki, A.; Maekawa, M.; Kuroda-Sowa, T. Crystal Structure and Carrier Transport Properties of a New Semiconducting 2D Coordination Polymer with a 3,5-Dimethylpiperidine Dithiocarbamate Ligand. *Chem. Commun.* **2013**, *49* (39), 4316−4318.
(54) Markvart, T.; Castañer, L. Semiconductor Materials and Modelling. In *Practical Handbook of Photovoltaics*; Elsevier: 2012; pp 33−62. .
(55) Gao, P.; Sun, X.-Y.; Liu, B.; Lian, H.-T.; Liu, X.-Q.; Shen, J.-S. Cu MOF-Based Catalytic Sensing for Formaldehyde. *J. Mater. Chem. C* **2018**, *6* (30), 8105−8114.
(56) Aguilera-Ruiz, E.; de la Garza-Galván, M.; Zambrano-Robledo, P.; Ballesteros-Pacheco, J. C.; Vazquez-Arenas, J.; Peral, J.; García-Pérez, U. M. Facile Synthesis of Visible-Light-Driven $Cu_2O/BiVO_4$ Composites for the Photomineralization of Recalcitrant Pesticides. *RSC Adv.* **2017**, *7* (73), 45885−45895.
(57) Yeşil, T.; Mutlu, A.; Siyahjani Gültekin, S.; Günel, Z. G.; Zafer, C. Enhanced Hole Mobility of P-Type Materials by Molecular Engineering for Efficient Perovskite Solar Cells. *ACS Omega* **2023**, *8* (30), 27784−27793.
(58) Talin, A. A.; Centrone, A.; Ford, A. C.; Foster, M. E.; Stavila, V.; Haney, P.; Kinney, R. A.; Szalai, V.; El Gabaly, F.; Yoon, H. P.; Léonard, F.; Allendorf, M. D. Tunable Electrical Conductivity in Metal-Organic Framework Thin-Film Devices. *Science* **2014**, *343* (6166), 66−69.
(59) Park, J.; Hinckley, A. C.; Huang, Z.; Feng, D.; Yakovenko, A. A.; Lee, M.; Chen, S.; Zou, X.; Bao, Z. Synthetic Routes for a 2D Semiconductive Copper Hexahydroxybenzene Metal−Organic Framework. *J. Am. Chem. Soc.* **2018**, *140* (44), 14533−14537.
(60) Han, W.; Shao, L.-H.; Sun, X.-J.; Liu, Y.-H.; Zhang, F.-M.; Wang, Y.; Dong, P.-Y.; Zhang, G.-L. Constructing Cu Ion Sites in MOF/COF Heterostructure for Noble-Metal-Free Photoredox Catalysis. *Appl. Catal. B: Environ.* **2022**, *317*, No. 121710.
(61) McDougald, R. N.; Chilukuri, B.; Jia, H.; Perez, M. R.; Rabaâ, H.; Wang, X.; Nesterov, V. N.; Cundari, T. R.; Gnade, B. E.; Omary, M. A. Molecular and Electronic Structure of Cyclic Trinuclear Gold(I) Carbeniate Complexes: Insights for Structure/Luminescence/Conductivity Relationships. *Inorg. Chem.* **2014**, *53* (14), 7485−7499.
(62) Zhang, T.; Sun, Z.; Li, S.; Wang, B.; Liu, Y.; Zhang, R.; Zhao, Z. Regulating Electron Configuration of Single Cu Sites via Unsaturated N,O-Coordination for Selective Oxidation of Benzene. *Nat. Commun.* **2022**, *13* (1), 6996.
(63) Huang, Q.-Q.; Lin, Y.-J.; Zheng, R.; Deng, W.-H.; Kashi, C.; Kumar, P. N.; Wang, G.-E.; Xu, G. Tunable Electrical Conductivity of a New 3D MOFs: Cu-TATAB. *Inorg. Chem. Commun.* **2019**, *105*, 119−124.

https://doi.org/10.1021/acs.chemmater.4c02974
Chem. Mater. 2025, 37, 1143−1153